

# Fundamental modes of swimming correspond to fundamental modes of shape: engineering I-, U-, and S-shaped swimmers

Sharan, Priyanka; Maslen, Charlie; Altunkeyik, Berk; Rehor, Ivan ; Simmchen, Juliane; Montenegro-Johnson, Tom

DOI:

[10.1002/aisy.202100068](https://doi.org/10.1002/aisy.202100068)

License:

Creative Commons: Attribution (CC BY)

*Document Version*

Publisher's PDF, also known as Version of record

*Citation for published version (Harvard):*

Sharan, P, Maslen, C, Altunkeyik, B, Rehor, I, Simmchen, J & Montenegro-Johnson, T 2021, 'Fundamental modes of swimming correspond to fundamental modes of shape: engineering I-, U-, and S-shaped swimmers', *Advanced Intelligent Systems*. <https://doi.org/10.1002/aisy.202100068>

[Link to publication on Research at Birmingham portal](#)

## General rights

Unless a licence is specified above, all rights (including copyright and moral rights) in this document are retained by the authors and/or the copyright holders. The express permission of the copyright holder must be obtained for any use of this material other than for purposes permitted by law.

- Users may freely distribute the URL that is used to identify this publication.
- Users may download and/or print one copy of the publication from the University of Birmingham research portal for the purpose of private study or non-commercial research.
- User may use extracts from the document in line with the concept of 'fair dealing' under the Copyright, Designs and Patents Act 1988 (?)
- Users may not further distribute the material nor use it for the purposes of commercial gain.

Where a licence is displayed above, please note the terms and conditions of the licence govern your use of this document.

When citing, please reference the published version.

## Take down policy

While the University of Birmingham exercises care and attention in making items available there are rare occasions when an item has been uploaded in error or has been deemed to be commercially or otherwise sensitive.

If you believe that this is the case for this document, please contact [UBIRA@lists.bham.ac.uk](mailto:UBIRA@lists.bham.ac.uk) providing details and we will remove access to the work immediately and investigate.

# Fundamental Modes of Swimming Correspond to Fundamental Modes of Shape: Engineering I-, U-, and S-Shaped Swimmers

Priyanka Sharan, Charlie Maslen, Berk Altunkeyik, Ivan Rehor, Juliane Simmchen,\* and Thomas D. Montenegro-Johnson

Hydrogels have received increased attention due to their biocompatible material properties, adjustable porosity, ease of functionalization, tuneable shape, and Young's moduli. Initial work has recognized the potential that conferring out-of-equilibrium properties to these on the microscale holds and envisions a broad range of biomedical applications. Herein, a simple strategy to integrate multiple swimming modes into catalase-propelled hydrogel bodies, produced via stop-flow lithography (SFL), is presented and the different dynamics that result from bubble expulsion are studied. It is found that for "Saturn" filaments, with active poles and an inert midpiece, the fundamental swimming modes correspond to the first three fundamental shape modes that can be obtained by buckling elastic filaments, namely, I, U, and S-shapes.

motors originates from exploiting various phenomena, including bubble propulsion, diffusiophoresis, electrophoresis, and Marangoni flow, among others. Some of the earliest researched artificial micromotors were bubble-driven, where gas bubbles are released from the micromotor body due to decomposition of  $\text{H}_2\text{O}_2$ .<sup>[1–5]</sup> More recently, interest in bubble propulsion has declined due, in part, to the rise of novel phoretic propulsion mechanisms,<sup>[6–8]</sup> but also because existing manufacturing techniques are able to produce few adaptable properties, such as programmability of trajectories, or complex shape designs. Indeed, the geometries of bubble-driven micromotors have been largely restricted

## 1. Introduction

Nanomotors and micromotors are self-propelling artificial machines that harvest energy from their environment (chemical, light, heat) and transform it into motion. The propulsion of

to tubes, or spherical particles, with notable exceptions including the stomatocytes, presented by the Wilson group, as one of the smallest bubble-driven micromotors.<sup>[9]</sup> Larger swimmers include cartridge-shaped polymer structures<sup>[10]</sup> and spherical micromotors,<sup>[11]</sup> while other complex geometries include spindle, drum, zigzag, and bilayer shapes<sup>[12]</sup> and helical motor bodies;<sup>[13]</sup> the performance of serrated swimmers, for example, was shown to depend significantly on geometry.<sup>[14]</sup> However, the previously used fabrication techniques including colloidal synthesis<sup>[9]</sup> and roll-up technology<sup>[2,15]</sup> are not capable of producing major shape variations or material composition of microswimmers, on-demand, to comply to a large variety of theoretically proposed designs.

From a hydrodynamical perspective, there are three aspects to bubble propulsion, which may be present in any given system. In the first stage, bubble growth causes the displacement of fluid. Due to the proximity of the swimmer to the bubble, this displacement is anisotropic, yielding a propulsive flow. This bubble may then eject from the swimmer, as in the propulsion of tubular microjets, and the swimmer is propelled forward at a velocity such that the net force on the bubble and swimmer is zero.<sup>[16]</sup> Alternatively, the growing bubble may violently collapse, creating a microjet of fluid perpendicular to the surface of the swimmer that impulsively propels the swimmer in the opposite direction over a very short interval.<sup>[17]</sup>


Gibbs et al.<sup>[18]</sup> presented a simple model based on the formation and release of oxygen bubbles that leads to a change in momentum, and used this model to describe the motion of spherical swimmers. Fomin et al.<sup>[19]</sup> fitted both ejection and

P. Sharan, J. Simmchen  
Chair of Physical Chemistry  
TU Dresden  
01062 Dresden, Germany  
E-mail: juliane.simmchen@tu-dresden.de

C. Maslen, I. Rehor  
Department of Chemical Engineering  
University of Chemistry and Technology  
Prague, Czech Republic

B. Altunkeyik, T. D. Montenegro-Johnson  
School of Mathematics  
University of Birmingham  
Edgbaston, Birmingham B15 2TT, UK

I. Rehor  
Institute of Organic Chemistry and Biochemistry of the  
Czech Academy of Sciences  
Flemingovo nám. 2, 160 00 Prague, Czech Republic

 The ORCID identification number(s) for the author(s) of this article can be found under <https://doi.org/10.1002/aisy.202100068>.

© 2021 The Authors. Advanced Intelligent Systems published by Wiley-VCH GmbH. This is an open access article under the terms of the Creative Commons Attribution License, which permits use, distribution and reproduction in any medium, provided the original work is properly cited.

DOI: 10.1002/aisy.202100068

growth models to experimental results, and found that they did not fully account for the propulsive force, as the swimming speeds and bubble ejection frequencies are underpredicted by these models. An explanation for this was found in the capillary force induced through the asymmetry of the tube shape; this asymmetry led to a momentum transfer, which is counteracted by a jet force yielding higher velocities. In a later study, the same author extended their considerations to the mixing effect from the bubble ejection.<sup>[15]</sup> Other approaches include considering bubble geometric asymmetry and buoyancy force; Li et al.<sup>[20]</sup> found that the buoyancy force deforms the bubble, and therefore influences bubble release. In contrast to these methodologies, Gallino et al.<sup>[21]</sup> assumed that bubbles in tubular microjets remain spherical while passing through the inside of the tube, due to the predominance of capillary effects. Working in the zero Péclet number limit, Boundary Element Methods were used to sequentially provide the gas concentration via solution of Laplace's equation, and use the resulting bubble growth as boundary conditions for solving the Stokes flow equations.

In this article, we introduce chemically driven, hydrogel microswimmers produced using stop-flow lithography (SFL).<sup>[22,23]</sup> a high throughput microfluidic technique for the production of micrometer scale ( $\sim 10$ – $1000\ \mu\text{m}$ ) hydrogels (microgels) of arbitrary 2D shapes. Exploiting laminar flow of multiple streams in microfluidic channels allows the production of microgels with discretely variable composition. The method allows the production of poly(ethylene glycol) diacrylate (PEGDA) microgels with active regions (containing catalase enzyme) and inactive regions (composed of pure PEGDA). The spatial location of the active and inactive regions, coupled with the shape design of the microgels, leads to different motion behaviors—stationary, ballistic, and rotation. These three modes of propulsion correspond to the first three shape/bending modes of an elastic filament: a zeroth mode filament (straight, I-shape) with two active caps is stationary by

symmetry, a filament bent into the first mode (one bend, U-shape) will translate but not rotate (by symmetry), and a filament bent in the second mode (two bends, S-shape) will rotate, as suggested in recent theoretical work on autophoretic swimmers.<sup>[24]</sup> It is expected, therefore, that this behavior may be recovered for a variety of propulsion mechanisms—modification of swimmer geometry, ultimately in an adaptable or programmable manner, may be used to control and modulate swimming behavior.

## 2. Results

A representative scheme of the production process in the SFL technique is shown in **Figure 1a,b**. The achieved structures are tens of micrometers in size (the size can be tuned by changing the magnification in **Figure 1a,b**). The successful incorporation of fluorescently labeled catalase in the hydrogel structure was proven by means of fluorescent microscopy, as well as by active bubble production after exposing the particles to peroxide fuel. The created bubbles increase the buoyancy of the hydrogel structures, so the motion is observed to be at the air–water interface, as commonly observed for bubble-driven motors.<sup>[25]</sup> A fraction of the particles with decreased to no activity were routinely observed sedimenting to the bottom surface, and are out of the focal plane and so unseen in the images. The active motility depends on the shape and enzyme distribution within the swimmers: two-component swimmers in a simple rod shape move ballistically (**Figure 1c, e**), while their three-component equivalents remain static while producing bubbles, which leads to fluid pumping instead, due to the higher symmetry of the system (**Figure 1d,f**). We found the catalase activity to be long lasting: when stored in the fridge ( $-20\ ^\circ\text{C}$ ), the particles could swim for about 14 days after fabrication, after which the activity declined noticeably.

The versatility of the SFL to flexibly change shapes during particle production was confirmed by exchanging the photomasks,

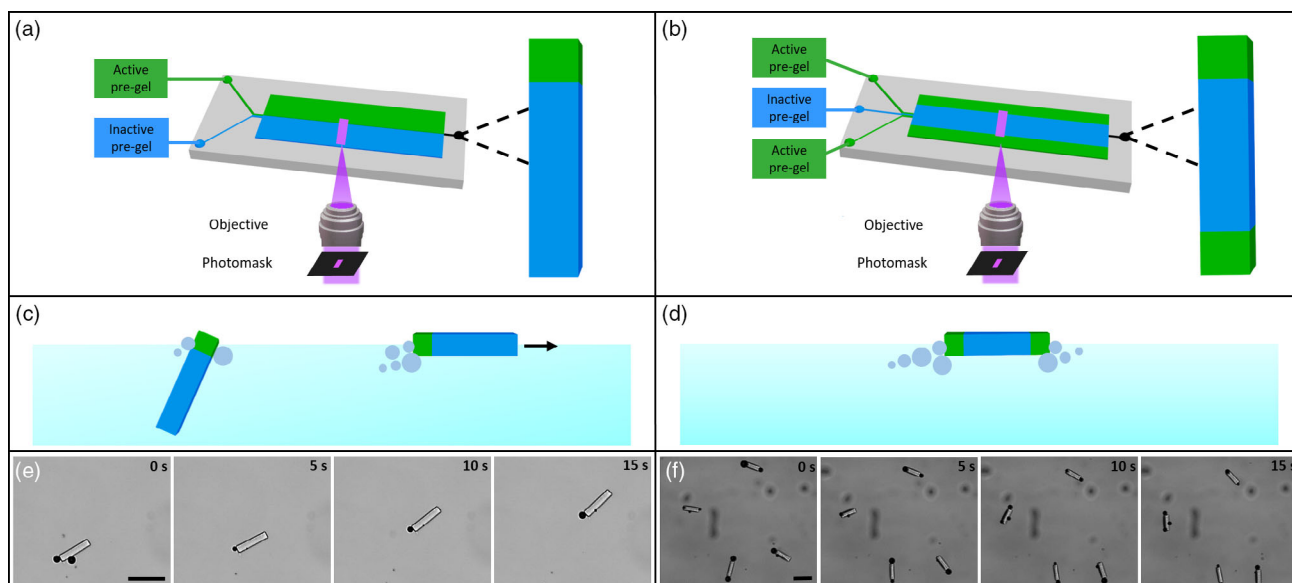


**Figure 1.** a) Fabrication principle of two component swimmers (further explanation in the text); b) fabrication principle of three component swimmers. c,d) Swimming principle at the air water interface of two and three component swimmers, respectively. e,f) Image sequence of bubble release versus motility, depending on the composition of the micromotors. Scale bar equals  $100\ \mu\text{m}$ .

and producing letters in the shape of U, I, and S (see **Figure 2** for the smaller microgel sizes and **Figure S1**, Supporting Information, for greater sizes). The shape in 3D is confirmed by means of scanning electron microscopy (SEM) images of freeze-dried microgels (**Figure 2**). The active and inactive regions in the swimmer body were indicated using dye labeling. Rhodamine-labeled catalase was used to label the enzyme-loaded region (active region) in the swimmer (indicated in red in **Figure 2**) and Fluorescein-*o*-acrylate was used to indicate the inactive regions of the enzyme (indicated in green in **Figure 2**). The thickness of the active region can be tuned easily by changing the flow rates of the active and inactive component with respect to each other. The active regions were kept small to control the position of bubbles effectively. A higher concentration of inactive component was chosen to increase the cross-linking density, which helped in preventing the diffusion of gas bubbles inside the inactive component, to an extent. Due to a two times lower PEGDA concentration in the active pregel composition, as compared with the inactive component, a slightly higher shrinkage at the edges of the fabricated letters was observed in the freeze-dried SEM samples.

We now analyze the periodic growth-collapse dynamics of the propulsive gas bubbles. This analysis comprises automated capture of the bubble radii as a function of time using custom routines (**Figure 3a–c**), together with a mathematical model for the bubble growth and a qualitative description of the collapse. The dynamics of microbubbles is dominated by surface tension<sup>[17]</sup> (i.e., the capillary number is small), and so the gas pressure  $P$  inside

the bubble may be well approximated by the Laplace law  $P = P_{\infty} + 2\sigma/r_b$ , for bubble radius  $r_b$ , and surface tension  $\sigma$ , and ambient pressure  $P_{\infty}$ . The gas inside the bubble obeys the ideal gas law

$$PV = nRT \quad (1)$$

where  $n$  is the number of moles of gas present in the bubble,  $T$  is the temperature in Kelvin (assumed constant), and  $R$  is the ideal gas constant. We assume that the bubble remains spherical, so that  $V = 4\pi r_b^3/3$ . Substituting these expressions into the ideal gas equation and taking the derivative with respect to time yields

$$\frac{1}{RT} \frac{d}{dt} \left[ \left( P_{\infty} + \frac{2\sigma}{r_b} \right) \frac{4\pi r_b^3}{3} \right] = \frac{dn}{dt} \quad (2)$$

so that the bubble growth dynamics are given by

$$\dot{r}_b = \frac{RT}{4\pi P_{\infty} r_b^2 + 4\sigma r_b/3} \frac{dn}{dt} \quad (3)$$

where  $dn/dt$  is the molar flux of gas into the bubble.

Under the simplest assumption, gas is produced at the catalytic surface at a constant rate, and moves immediately into the bubble, rather than diffusing through the surrounding solute—i.e., the flux of gas into the bubble is confined to a thin region at the catalytic surface. In this case, the molar flux  $dn/dt = Q$ , for some constant  $Q$ . Substituting Equation (3), we find

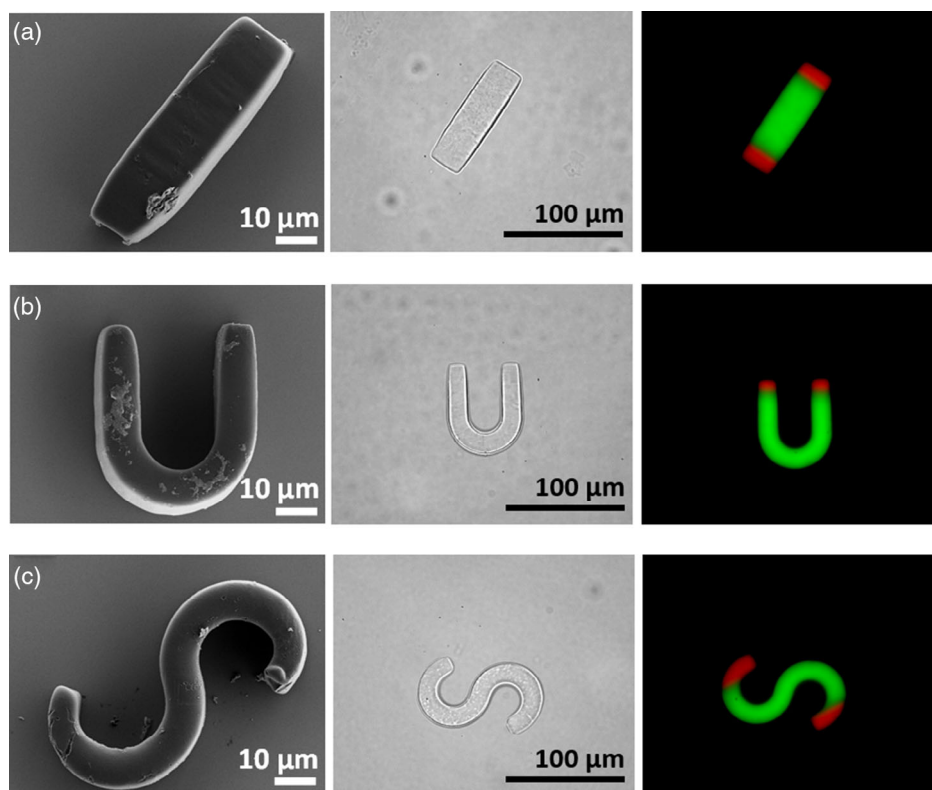


**Figure 2.** SEM micrograph, optical micrograph, and overlaid micrograph of different fluorescent channels, indicating the passive swimmer body (green) and the active, enzyme incorporating regions (red), respective of a) I-shaped swimmers, b) U-shaped swimmers, and c) S-shaped swimmers.

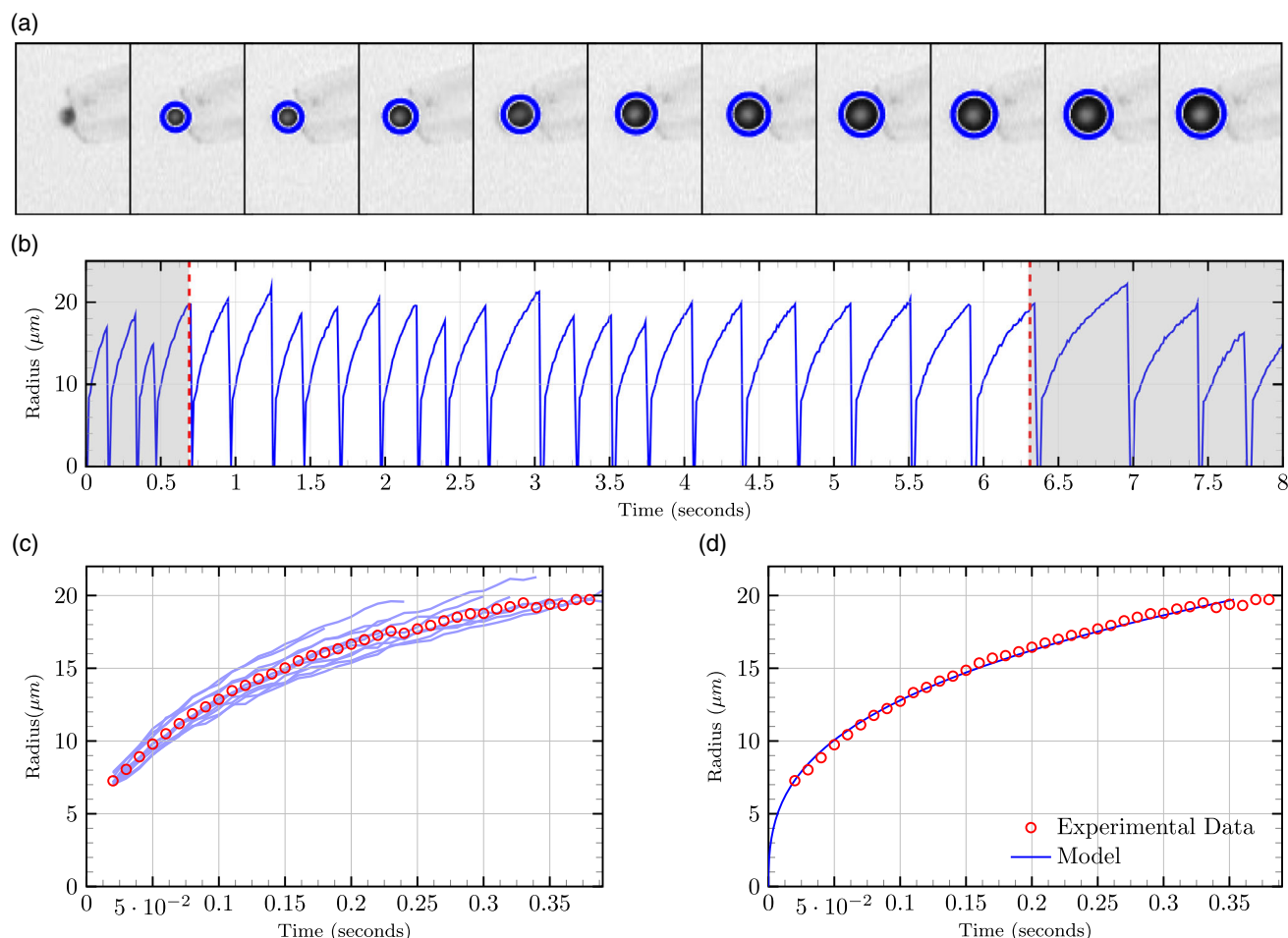


**Figure 3.** Analysis of the growth of a single bubble. a) Frame-by-frame of a single growing bubble over an entire growth cycle. The blue circle denotes the extent of the bubble, found via circular Hough transform. b) The radius of a single bubble as a function of time over multiple growth/collapse cycles. A subregion of clean data is selected to be used for phase averaging. c) Phase-averaged growth of the bubble, to be compared with modeling results. d) Model with a single parameter, the constant molar flux, fitted to experimental data, showing good agreement.

$$\dot{r}_b = \frac{RT}{4\pi P_\infty r_b^2 + 4\sigma r_b/3} \Rightarrow \frac{P_\infty}{3} r_b^3 + \frac{2\sigma}{3} r_b^2 = \frac{RTQ}{4\pi} t \quad (4)$$

for time  $t$ , where we have used the initial condition  $r = 0$  at  $t = 0$ . While this equation is not analytically invertible, it is a simple matter to numerically find  $r_b(t)$  for a given  $Q$ . Taking values of  $R = 8.314 \text{ J mol}^{-1} \text{ K}^{-1}$ ,  $T = 293 \text{ K}$ ,  $\sigma = 7.2 \times 10^{-2} \text{ Nm}^{-1}$ , and  $P_\infty = 1$  atmosphere =  $101325 \text{ Nm}^{-2}$ , we find a value of  $Q \approx 8.45 \times 10^{-13} \text{ mol s}^{-1}$ , fitting our model well to phase-averaged experimental data (Figure 3d). There is significant variance in this fitted parameter from cycle to cycle, with slower growth phases typically having  $Q \approx 6 \times 10^{-13} \text{ mol s}^{-1}$  and faster growing bubbles around  $Q \approx 1.2 \times 10^{-12} \text{ mol s}^{-1}$ .

This variation in the flux occurs from one cycle to the next stochastically, although we note a long-time (multicycle) trend of decreasing maximum bubble radius (Figure 4a) and slower bubble growth (Figure 4b). This long-time trend indicates that the molar flux of gas into the bubble decays slowly over time. Possible explanations for this include local depletion of solute near the swimmer and degradation of the catalytic enzyme.

As this is true for both pumps and translators, which can move into areas replete with solute, we conclude that this decay is at least, in part, due to enzymatic degradation.

Finally, we examine the cause of the bubble collapse. As the bubble grows, the gas pressure lowers until it is similar to the pressure of the liquid, whereupon fluctuations can provide enough of a kick for collapse.<sup>[17]</sup> This point can be estimated via the Blake critical radius<sup>[26]</sup>

$$R_c = \left[ \frac{9m_g RT}{8\pi\sigma} \right]^{1/2} \quad (5)$$

The mass of gas  $m_g$  is approximated by the average flux in one of our bubbles  $Q \approx 8.45 \times 10^{-13} \text{ mol s}^{-1}$  multiplied by the average time of a growth-collapse cycle  $\approx 0.5 \text{ s}$  using the data in Figure 3b. The critical radius is thus around  $70 \mu\text{m}$ , while we see our bubbles collapsing at around  $20 \mu\text{m}$ . Thus, it is likely that the cause of collapse in our case is interaction between the bubble and the air–water interface.



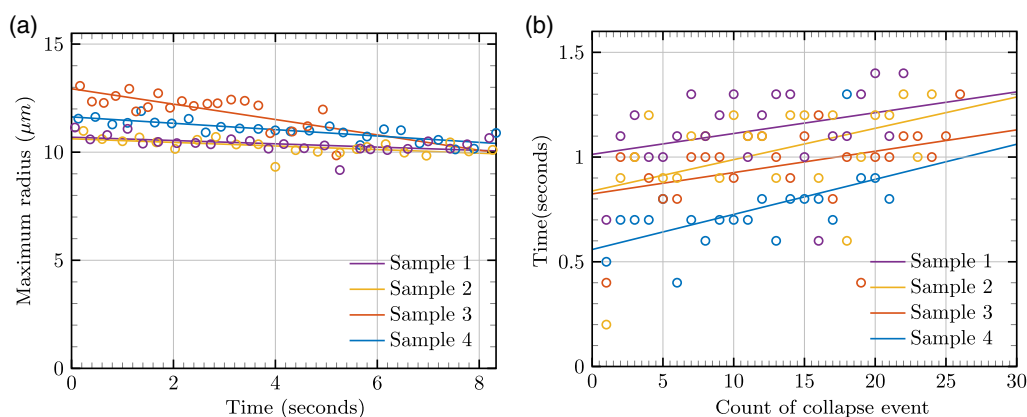


**Figure 4.** Multicycle analysis of four bubbles at different locations. a) Steady (linear) decay of the maximum bubble radius over time, indicating decay of the catalytic enzyme, or local depletion of solute. b) Period between collapse events, showing a steady increase.

We conclude with the observation that the effect of a collapsing bubble near a solid body is well documented, and results in a small jet of fluid that provides an impulsive force to the swimmer.<sup>[27]</sup> Thus, the bubble growth phase provides a steady propulsive force, while the collapse provides a sudden impulse from the ensuing microjet. We now characterize these dynamics more thoroughly.

When swimmers in the “I,” “U,” and “S” shapes were dispersed in  $\text{H}_2\text{O}_2$  fuel, the observed swimmer dynamics was highly shape dependent (Figure S2, Supporting Information). In the “I” configuration, enzyme is located at both poles, and by symmetry the propulsive forces arising from the bubbles are equal and opposite, resulting in no net motion and a

pumping “stresslet”-like flow (Figure 5a and Figure S9, Supporting Information, for theta and displacement vs time plot of Figure 5 particles, more examples in Figure S3 and S4, Video S1, S2, Supporting Information). Typically, a U-shaped swimmer prefers to propel ballistically, owing to its geometry (Figure 5b, and more examples in Figure S5, S6, Supporting Information). The gas bubbles located at the two poles of the “U” configuration impart a propulsive force in the same direction as each other, which is balanced by the drag force of the swimmer moving forward.

In the case of a perfectly manufactured S-shaped swimmer, propulsive forces are again equal and opposite, so that no net force is exerted on the fluid that needs to be balanced by drag

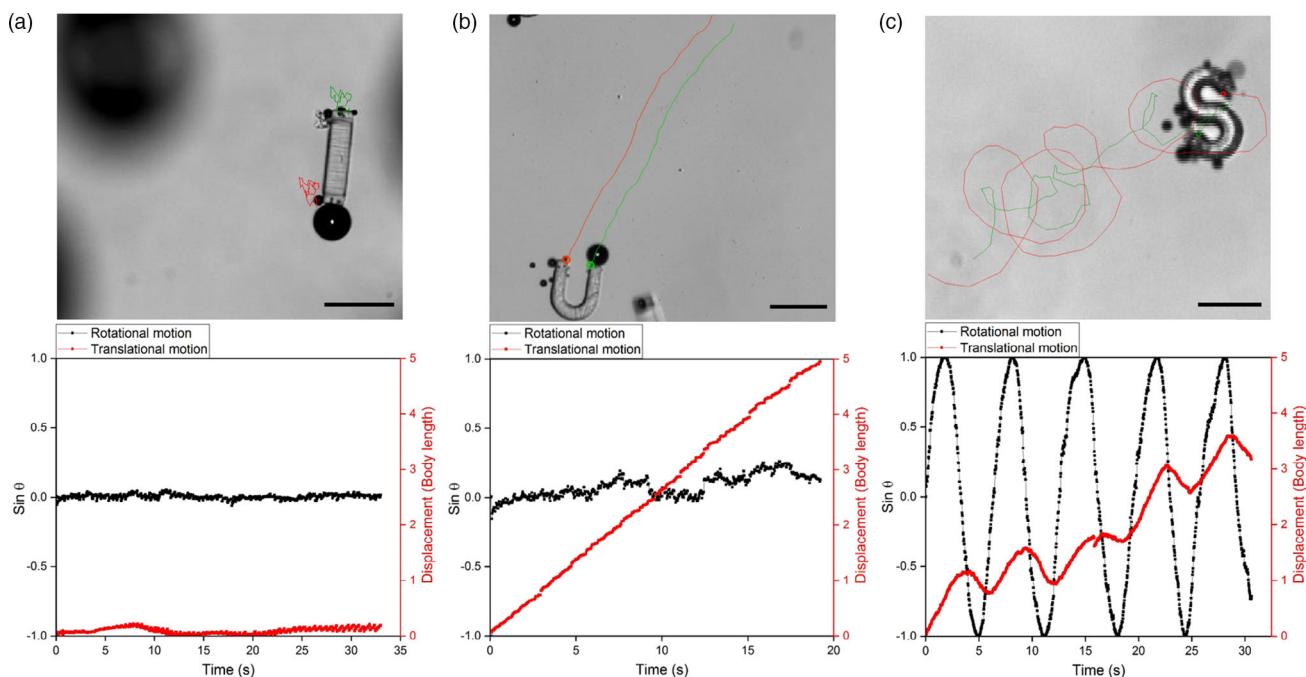


**Figure 5.** Typical motion patterns of the differently shaped particles: micrographs and corresponding analysis [ $\sin \theta$  and displacement plotted versus time] of a) pumping of I-shaped swimmers, b) translating movement of U-shaped swimmers, and c) rotating S-shaped swimmers. Scale bar equals 150  $\mu\text{m}$ .

arising from translation. However, the displacement of the forces about the center results in a torque that is balanced by the rotation of the swimmer. In addition, small differences in manufacturing and indeed inherent randomness in the bubble nucleation sites will almost always lead to a slight rotational asymmetry, in which case the S-shaped swimmer will also translate while rotating (Figure 5c, more examples in Figure S7 and S8, Supporting Information). In summary, a U-shape behaves as a propeller, an I-shape as a pump, and a S-shape as a moving rotor.

Localization of the bubbles on the microgel surfaces varies between the individual microgels. We ascribe this to the stochasticity of the bubble nucleation and growth, and the fact that surface irregularities, some small local defects, may foster the bubble nucleation at a particular spot. These nucleation spots on the active microgel surface remain unchanged over the course of the experiment involving hundreds/thousands of bubbles formed. Different localizations of the bubble nucleation sites result in different microgel modes of motion. For example, in the “I” configuration, if additional bubbles are located at the sides of the swimmer body, in addition to the gas bubbles at the poles, the swimmer rotates and translates (Figure 6a, Figure S10, Supporting Information, for theta and displacement versus time plot of Figure 6 particles and Video S3, Supporting Information). The interplay of bubble growth and collapse at different locations results in a different motion pattern in this case. It is observed that a “U” configuration in which only a single pole is active can force the fabricated structure to rotate, in addition to translation (Figure 6b). The location of the gas bubble only at one pole results in unbalancing of the propulsive force (which is acting on only one side in this case as compared to when both the poles

are active), producing a moment about the swimmer’s center of drag that results in rotation. The ballistic motion of the U-shaped swimmer is compromised due to additional rotation of the swimmer; the rotation observed, however, was not as fast as that observed in the case of the “S” configuration. Since the motion of an S-shaped swimmer already has a translational and rotational component, the qualitative dynamics of its trajectory remain unaffected by imperfections, such as having only a single active cap (Figure 6c); even if gas bubbles are only produced from one of the poles, the rotating motion pattern is conserved (due to the moment of the force about the swimmer’s center of drag), and merely the pivotal point and the periodicity are shifted.

### 3. Discussion

A considerable body of research has focused on the fabrication of micromotors with controllable shapes and sizes. Here, we used SFL as a high throughput microfluidic technique to engineer micromotors. This technique provides an edge over other methods in terms of freedom in shape selection and in controlling the active regions in the fabricated geometries. Exploiting the laminar flow in the low Reynolds number regime in the microfluidics channels, we fabricated I-, U-, and S-shaped configuration with active regions confined at the two poles of the shapes. The spatial confinement of the active component was confirmed by labeling the enzyme with a fluorescent dye. The active motion pattern of these configurations was witnessed after mixing them with  $\text{H}_2\text{O}_2$ . Oxygen bubbles generated due to decomposition of  $\text{H}_2\text{O}_2$  result in efficient bubble propulsion.

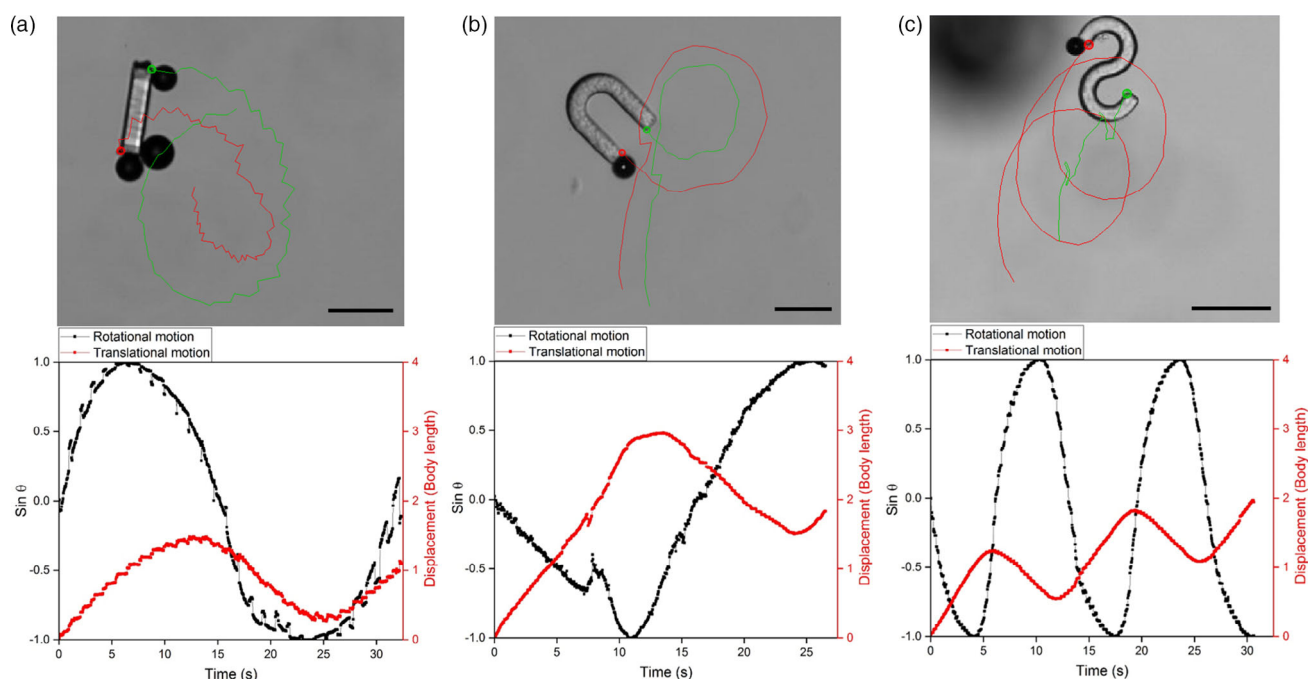


**Figure 6.** Motion patterns of the differently shaped particles caused by the influences described earlier: micrographs and corresponding analysis [ $\sin \theta$  and displacement plotted versus time] of a) partial rotation, partial translation of I-shaped swimmers, b) partial rotation, partial translation of U-shaped swimmers, and c) rotating translation of S-shaped swimmers. Scale bar equals 150  $\mu\text{m}$ .

The interplay of shape, catalytic decomposition of solute, and resultant bubble growth and collapse driving propulsive fluid flows determines the trajectories of the fabricated configurations. Bubbles collapsing at the two poles of an U-shaped configuration contribute to ballistic motion, while the higher symmetry of the I-shaped swimmer leads to these propulsive forces on the swimmer cancelling so that the shape functions as a pump. In the S-shaped microgel, although rotational symmetry means that the forces are equal and opposite, cancelling ballistic motion, their displacement allows them to exert a couple on the swimmer, which results in rotation. This rotational symmetry is not perfect, and as a result the S-shape also exhibits some translation, resulting in a moving rotor that may be able to act as an excellent microscale mixer.

## 4. Conclusion

In this work, we could show that different configurations of hydrogel microswimmers can achieve a set of swimming behaviors dependent on their geometries. As predicted theoretically,<sup>[24]</sup> a straight I-shaped geometry can either act as a pump or as a ballistic swimmer, having two or only a single catalytic patch, respectively. U-shaped hydrogels are dominantly translators, while S-shapes are commonly rotating. As bubble propulsion is strongly dependent on the local surface properties (e.g., cavities, or nucleation points), we find a rather large proportion of microswimmers deviating from the expected swimming modes, resulting in a broad spectrum of swimming behaviors. In the future, the implementation of shape changing materials can lead to the development of multifunctional actuators that respond to different stimuli and perform specific tasks depending on their environment. In addition, the use of hydrogels will facilitate the use of a variety of enzymes operating on base of different substrates and therefore enable the use of different fuels, which might lead to a platform technology.

## 5. Experimental Section

**Materials:** PEGDA ( $M_n = 700$ ), Lithium phenyl-2,4,6-trimethylbenzoyl-phosphinate (LAP), Catalase from bovine liver (lyophilized powder)  $\geq 10\,000$  units  $\text{mg}^{-1}$  protein, Fluorescein *o*-acrylate, Rhodamine B isothiocyanate (RITC) Tween 20, Glycerol, and Hydrogen peroxide were purchased from Sigma-Aldrich. SYLGARD 184 Silicone Elastomer Kit was purchased from Dow-Corning.

**Labeling Catalase with RITC:** Catalase (1 mg) was dissolved in phosphate-buffered saline (PBS) (1 mL) and a solution of RITC (2  $\mu\text{L}$  of stock solution of concentration  $0.2\text{ mg mL}^{-1}$ ) was added. The mixture was gently stirred for 4 h and subsequently dialyzed against 200 mL PBS (three times, buffer was exchanged every 6 h). The final volume of the solution was 1.2 mL. The solution was divided into 150  $\mu\text{L}$  aliquots and stored at  $-20^\circ\text{C}$  for subsequent use.

**Pregel Compositions:** Active pregel: LAP (10 mg) was dissolved in 650  $\mu\text{L}$  of PBS buffer. Catalase (12.5 mg) was added to the mixture and dissolved by vortexing, followed by PEGDA (200  $\mu\text{L}$ ) addition. Then the solution of Rhodamine-labeled catalase, as received in the labeling step was added (150  $\mu\text{L}$ ). The resulting mixture was vortexed and spinned down (10 000 g, 5 min) to remove dispersed dirt. Fresh compositions were prepared before each use.

**Inactive pregel:** Similar to active pregel composition, LAP (10 mg) was dissolved in 550  $\mu\text{L}$  of PBS buffer followed by PEGDA (400  $\mu\text{L}$ ) addition. Then, 50  $\mu\text{L}$  of Fluorescein *o*-acrylate (8  $\text{mg mL}^{-1}$  in DMSO) was added.

This mixture was sonicated well and centrifuged for 5 min before use. Fresh mixtures were prepared before each use.

**Microfluidic Channel Production:** Polydimethylsiloxane (PDMS) microfluidic (depth = 30  $\mu\text{m}$ ) channels were produced as follows. Silicon wafers with SU-8 photoresist positive relief channels (Microchem) were used as masters, having lateral dimensions of  $300\text{ }\mu\text{m} \times 15\,000\text{ }\mu\text{m}$  and the height 30 and 50  $\mu\text{m}$  for production of microgels of corresponding thickness. Silicone elastomer base (35 g) and curing agent (5 g) from the Elastomer Kit were mixed well and centrifuged at 15 000 g for 20 min. The mixture was then poured over the silicon wafer and degassed under vacuum (40 mbar, 20 min). The PDMS was cured by storing the wafer at  $70^\circ\text{C}$  overnight after which it was cut and removed from the wafer and divided into individual pieces, each containing one channel. Using a biopsy needle, a 1 mm hole was punctured through the PDMS pieces at the end of each inlet channel and at the opposite, outlet, end of the main channel. Separately, glass slides were spin-coated with PDMS with a 10:1 ratio of elastomer:base. The glass slides were partially cured by storing them at  $70^\circ\text{C}$  for 35 min. After partial curing, the PDMS pieces were placed, channel side down, on the PDMS side of the slides and these were then cured at  $70^\circ\text{C}$  overnight. Three inlet adapters were made using flattened 1 mm diameter syringe needles with Luer adaptors and inserted in the inlet holes. A 1 mm diameter capillary was inserted into the outlet and fed into a polymerase chain reaction (PCR) tube containing 1 wt% Tween 20.

**SFL:** The SFL method is adapted from that presented by Dendukuri et al.<sup>[22]</sup> The active pregel solution (50  $\mu\text{L}$ ) was loaded into each of the two outer inlets and 50  $\mu\text{L}$  of the inactive pregel was loaded into the inner inlet. The pregels were pumped into the channel using compressed  $\text{N}_2$ , regulated to 0.4–0.6 psi using a pressure regulator. One pressure regulator was used for the outer inlets and another for the central inlet. This allowed the dimensions of the outer, sheath, flows to be regulated manually. Both regulator outputs were connected to synchronized three-way solenoid valves which allowed rapid switching between input atmospheric pressure. The channels were placed on the stage of an inverted microscope (Nikon Ti-U). UV light passed through a photomask in the focal plane of the microscope objective such that it illuminated the channel in the shape given by the photomask. The shutter of the UV source and the solenoid valves were controlled by a Raspberry Pi, programmed to cycle in the following progression: flow—pregel is pumped through the channel, stop—the flow is stopped, print—UV light illuminates the channel. The UV light induced polymerization and cross-linking of the pregel in the illuminated region, producing microgels with shapes defined by the photomask and a depth slightly less than the depth of the channel ( $\approx 27\text{ }\mu\text{m}$ ). By controlling the dimensions of the sheath flow and the position of the illuminated area, the active and inactive compositions were localized to predesigned regions of the microgel. The stop—print—flow cycle could be repeated up to 4 Hz and, with 50  $\mu\text{L}$  of pregel in each inlet, was used to produce some 14 000 microgels within an hour. The photomasks and collection PCR tubes were exchanged within the synthesis, providing separate samples from the same set of pregel. After synthesis, the microgels were sedimented (10 min) washed five times with PBS (220  $\mu\text{L}$  concentrated to 20  $\mu\text{L}$ ), to remove the excess of catalase. Washed microgels were stored at  $-20^\circ\text{C}$  for subsequent use.

**Motion Studies and Analysis:** Motion studies were performed in specifically designed wells. Typically, plastic washers of 2 mm height and 10 mm inner diameter were stuck on to glass slides using spin-coated PDMS as an inert glue, to render the system optically transparent. This entire assembly was then cured at  $70^\circ\text{C}$  for 12 h. The fabricated wells were filled with an aqueous 2.5 wt%  $\text{H}_2\text{O}_2$  solution containing 7.5 wt% Glycerol and subsequently swimmers were added. The motion and bubbling of microswimmers was recorded using an attached camera to an inverted Nikon (Ti-U) microscope. The recordings were generated at 30 frames per second. The videos were analyzed using Tracker software.

**SEM:** Droplets of water containing fabricated microswimmers were cast on silicon wafer and shock frozen using liquid  $\text{N}_2$ . Afterward, these frozen droplets were subjected to freeze drying. SEM images were obtained after sputtering a 5 nm thin Au-Pd layer on the silicon sample holders, using a Zeiss Gemini SEM 300 instrument using a 3 kV electron beam.



**Fluorescence Imaging:** Fluorescence images were captured on an inverted Nikon (Ti-U) microscope using green and red channels of light. The obtained images (one in green channel and the other in red channel) were subsequently overlayed in ImageJ to obtain the final images.

**Image Analysis of Bubbles:** Videomicroscopy data were first imported into Matlab, whereupon we selected a small region of interest (ROI) containing a single bubble. We then performed a frame-by-frame analysis on this ROI to find the radius of the bubble for each frame. A circular Hough Transform was used within the built-in function `imfindcircles` to give the bubble radius (Figure 3a). As the interior of the bubble appears consistently darker than the surroundings, erroneous results (most common when the bubble is small or has just collapsed) were removed by ensuring that the standard deviation of the pixels inside the circle is below a threshold. The radius as a function of time was then plotted as a periodic signal (Figure 3b). A region of interest of clean data was selected from the periodic signal (Figure 3b, between the red dashed lines), and the locations of the collapse event (to the nearest frame) were used to “phase-average” the signal (Figure 3c), to give an averaged data set against which to compare our model.

## Supporting Information

Supporting Information is available from the Wiley Online Library or from the author.

## Acknowledgements

P.S., C.M., and B.A. contributed equally to this work. J.S. and P.S. acknowledge a Freigeist grant (no. 91619) from Volkswagen foundation. P.S. also acknowledges Erasmus+ Staff Mobility program. B.A. and T.D.M.-J. gratefully acknowledge support from a Leverhulme Trust Research Leadership Award to T.D.M.-J., and B.A. also acknowledges support from the EPSRC for funding via a Ph.D. scholarship (grant no. EP/N509590/1). I.R. acknowledges the UCT Prague D. Prochazkova Initiation Grant and the Czech Academy of Sciences J.E. Purkyne Fellowship. C.M. acknowledges the UCT Prague grant of Specific University Research (grant no. A1\_FCHI\_2020\_005).

## Conflict of Interest

The authors declare no conflict of interest.

## Data Availability Statement

Raw data is available from the authors upon request.

## Keywords

active matter, bubble-driven micromotors, enzymes, microswimmers, stop-flow lithography

Received: April 20, 2021

Revised: June 21, 2021

Published online:

- [1] R. F. Ismagilov, A. Schwartz, N. Bowden, G. M. Whitesides, *Angew. Chem. Int. Ed.* **2002**, *41*, 652.
- [2] S. Sanchez, A. A. Solovev, S. M. Harazim, O. G. Schmidt, *J. Am. Chem. Soc.* **2011**, *133*, 701.
- [3] W. Gao, S. Sattayasamitsathit, A. Uygun, A. Pei, A. Ponedal, J. Wang, *Nanoscale* **2012**, *4*, 2447.
- [4] J. Simmchen, V. Magdanz, S. Sanchez, S. Chokmaviroj, D. Ruiz-Molina, A. Baeza, O. Schmidt, *RSC Adv.* **2014**, *4*, 20334.
- [5] P. Sharan, A. Nsamela, S. C. Leshner-Perez, J. Simmchen, *Small* **2021**, *17*, 2007403.
- [6] M. Kuron, P. Kreissl, C. Holm, *Acc. Chem. Res.* **2018**, *51*, 2998.
- [7] J. Bastos-Arrieta, C. Bauer, A. Eychmuller, J. Simmchen, *J. Chem. Phys.* **2019**, *150*, 144902.
- [8] L. Xu, F. Mou, H. Gong, M. Luo, J. Guan, *Chem. Soc. Rev.* **2017**, *46*, 6905.
- [9] L. K. Abdelmohsen, M. Nijemeisland, G. M. Pawar, G.-J. A. Janssen, R. J. Nolte, J. C. van Hest, D. A. Wilson, *ACS Nano* **2016**, *10*, 2652.
- [10] Y. Su, Y. Ge, L. Liu, L. Zhang, M. Liu, Y. Sun, H. Zhang, B. Dong, *ACS Appl. Mater. Interfaces* **2016**, *8*, 4250.
- [11] S. J. Ebbens, J. R. Howse, *Langmuir* **2011**, *27*, 12293.
- [12] C. Zhou, P. Zhu, Y. Tian, M. Xu, L. Wang, *ACS Nano* **2019**, *13*, 6319.
- [13] Y. Yu, L. Shang, W. Gao, Z. Zhao, H. Wang, Y. Zhao, *Angew. Chem. Int. Ed.* **2017**, *129*, 12295.
- [14] D. Li, Y. Liu, Y. Yang, Y. Shen, *Nanoscale* **2018**, *10*, 19673.
- [15] L. Soler, V. Magdanz, V. M. Fomin, S. Sanchez, O. G. Schmidt, *ACS Nano* **2013**, *7*, 9611.
- [16] J. Li, G. Huang, M. Ye, M. Li, R. Liu, Y. Mei, *Nanoscale* **2011**, *3*, 5083.
- [17] J. Zhang, X. Zheng, H. Cui, Z. Silber-Li, *Micromachines* **2017**, *8*, 123.
- [18] J. G. Gibbs, Y.-P. Zhao, *Appl. Phys. Lett.* **2009**, *94*, 163104.
- [19] V. M. Fomin, M. Hippler, V. Magdanz, L. Soler, S. Sanchez, O. G. Schmidt, *IEEE Trans. Robot.* **2014**, *30*, 40.
- [20] L. Li, J. Wang, T. Li, W. Song, G. Zhang, *Soft Matter* **2014**, *10*, 7511.
- [21] G. Gallino, F. Gallaire, E. Lauga, S. Michelin, *Adv. Funct. Mater.* **2018**, *28*, 1800686.
- [22] D. Dendukuri, S. S. Gu, D. C. Pregibon, T. A. Hatton, P. S. Doyle, *Lab Chip* **2007**, *7*, 818.
- [23] I. Rehor, C. Maslen, P. G. Moerman, B. G. Van Ravensteijn, R. Van Alst, J. Groenewold, H. B. Eral, W. K. Kegel, *Soft Robotics* **2021**, *8*, 10.
- [24] T. D. Montenegro-Johnson, *Phys. Rev. Fluids* **2018**, *3*, 062201.
- [25] J. Simmchen, A. Baeza, D. Ruiz-Molina, M. Vallet-Regi, *Nanoscale* **2014**, *6*, 8907.
- [26] F. Hegedus, *Ultrasonics* **2014**, *54*, 1113.
- [27] J. R. Blake, D. M. Leppinen, Q. Wang, *Interface Focus* **2015**, *5*, 20150017.